SURFACE CHEMISTRY

Covalent surface modifications and superconductivity of two-dimensional metal carbide MXenes

Vladislav Kamysbayev[1], Alexander S. Filatov[1], Huicheng Hu[1], Xue Rui[2], Francisco Lagunas[2], Di Wang[1], Robert F. Klie[2], Dmitri V. Talapin[1,3]*

Versatile chemical transformations of surface functional groups in two-dimensional transition-metal carbides (MXenes) open up a previously unexplored design space for this broad class of functional materials. We introduce a general strategy to install and remove surface groups by performing substitution and elimination reactions in molten inorganic salts. Successful synthesis of MXenes with oxygen, imido, sulfur, chlorine, selenium, bromine, and tellurium surface terminations, as well as bare MXenes (no surface termination), was demonstrated. These MXenes show distinctive structural and electronic properties. For example, the surface groups control interatomic distances in the MXene lattice, and $Ti_{n+1}C_n$ (n = 1, 2) MXenes terminated with telluride (Te^{2-}) ligands show a giant (>18%) in-plane lattice expansion compared with the unstrained titanium carbide lattice. The surface groups also control superconductivity of niobium carbide MXenes.

Two-dimensional (2D) transition-metal carbides and nitrides (MXenes) (*1*) have been actively studied for applications in supercapacitors (*2*), batteries (*3*), electromagnetic interference shielding (*4*), composites (*5*, *6*), and catalysts (*7*). MXenes are typically synthesized from the corresponding MAX phases (Fig. 1A), where M stands for the transition metal (e.g., Ti, Nb, Mo, V, W, etc.) and X stands for C or N, by selectively etching the main group element A (e.g., Al, Ga, Si, etc.). The etching is usually performed in aqueous hydrofluoric (HF) solutions, rendering MXenes terminated with a mixture of F, O, and OH functional groups, commonly denoted as T_x. These functional groups can be chemically modified, unlike the surfaces of other 2D materials such as graphene and transition-metal dichalcogenides. Recent theoretical studies predict that selective terminations of MXenes with different surface groups can lead to remarkable properties, such as opening or closing bandgap (*8*), room-temperature electron mobility exceeding 10^4 $cm^2/V{\cdot}s$ (*9*), widely tunable work functions (*10*), half-metallicity, and 2D ferromagnetism (*11*). Covalent functionalization of MXene surfaces is expected to uncover new directions for rational engineering of 2D functional materials.

The surface of MXene sheets is defined during MAX phase etching. Electrochemical and hydrothermal methods have been recently applied for etching MAX phases without resorting to HF solutions, but the use of aqueous solutions introduces a mixture of Cl, O, and OH surface groups (*12*, *13*). The etching of Ti_3AlC_2 MAX phase in molten $ZnCl_2$ and several other Lewis acidic molten salts above 500°C results in $Ti_3C_2Cl_2$ MXene with a pure Cl termination (*14*, *15*). Because etching of MAX phases in molten salts eliminates unwanted oxidation and hydrolysis, we used a variation of this method for synthesis of $Ti_3C_2Cl_2$, Ti_2CCl_2, and Nb_2CCl_2 MXenes in $CdCl_2$ molten salt (figs. S1 to S5). Moreover, the use of Lewis acidic $CdBr_2$ allowed us to extend the molten salt etching route beyond chlorides to prepare the first Br-terminated $Ti_3C_2Br_2$ and Ti_2CBr_2 MXenes (Fig. 1, B and C, and figs. S6 and S7). The morphology, structure, and composition of all newly synthesized MXenes were characterized using high-resolution scanning transmission electron microscopy (STEM), Raman spectroscopy, and a combination of x-ray methods, including energy-dispersive elemental mapping, diffraction (XRD), atomic pair distribution function (PDF), fluorescence, extended x-ray absorption fine structure (EXAFS), and photoelectron spectroscopy (XPS).

We show that Cl-terminated and especially Br-terminated MXenes can efficiently engage in a new type of surface reaction wherein halide ions exchange for other atoms and functional groups. The exchange reactions enable unprecedented control over the surface chemistry, structure, and properties of MXene materials.

The transition-metal atoms from the outer layers of MXene sheets (Ti, Mo, Nb, and V) form relatively weak M-Cl and M-Br bonds, in comparison to M-F and M-OH bonds typical for MXenes with T_x surface groups. This point can be demonstrated by the enthalpies of formation for $TiBr_4$ (−617 kJ mol^{-1}) and $TiCl_4$ (−804 kJ mol^{-1}) versus TiF_4 (−1649 kJ mol^{-1}), as well as by direct comparison of the bond energies (table S1). Strong Ti-F and Ti-O bonds make it difficult to perform any postsynthetic covalent surface modifications of MXenes (*16*). In contrast, Cl- and Br-terminated MXenes with labile surface bonding act as versatile synthons for further chemical transformations.

MXene surface exchange reactions typically require temperatures of 300° to 600°C, which are difficult to achieve using traditional solvents. We instead used molten alkali metal halides as solvents with unmatched high-temperature stability, high solubility of various ionic compounds, and wide electrochemical windows (*17*–*19*). For example, $Ti_3C_2Br_2$ MXene (Fig. 1B) dispersed in CsBr-KBr-LiBr eutectic (melting point: 236°C) reacted with Li_2Te and Li_2S to form Ti_3C_2Te (Fig. 1D and figs. S8 to S10) and Ti_3C_2S (Fig. 1E and fig. S11) MXenes, respectively. The reactions of $Ti_3C_2Cl_2$ and $Ti_3C_2Br_2$ with Li_2Se, Li_2O, and $NaNH_2$ yielded Ti_3C_2Se, Ti_3C_2O, and $Ti_3C_2(NH)$ MXenes, respectively (figs. S12 to S16). The multilayers of $Ti_3C_2T_n$ MXenes (T = Cl, S, NH) were further treated with n-butyl lithium (n-BuLi) resulting in Li^+ intercalated sheets (fig. S17) with a negative surface charge (Fig. 2A and fig. S18). Subsequent dispersion in a polar organic solvent such as N-methyl formamide (NMF) resulted in stable colloidal solutions of single-layer flakes (Fig. 2, B and C). Raman spectroscopy and elemental analysis showed that delaminated MXenes preserve their original T_n surface groups (figs. S18 to S20). The x-ray diffraction pattern of spin-coated films showed a single (0002) diffraction peak corresponding to the center-to-center separation (d) between two adjacent MXene sheets (Fig. 2D). The absence of $(10\bar{l})$ and $(11\bar{2}0)$ reflections is consistent with the alignment of delaminated flakes parallel to the substrate (*20*), which is also confirmed by the grazing incidence wide-angle x-ray scattering patterns (fig. S19).

Similar covalent surface modifications were achieved for Ti_2CCl_2, Ti_2CBr_2, and Nb_2CCl_2 MXenes (Fig. 3A and figs. S21 to S34). The ability to perform surface exchange reactions on the thinnest MXenes demonstrated that the 2D sheets remained intact during all stages of the transformation. The exact metal to surface group elemental ratios for newly synthesized MXenes were near the expected values, as summarized in table S2.

The reactions of $Ti_3C_2Br_2$ and Ti_2CBr_2 with LiH at 300°C produced bare $Ti_3C_2\square_2$ (Fig. 1F and fig. S14) and $Ti_2C\square_2$ MXenes (fig. S21), where □ stands for the vacancy site. Because H-terminations are difficult to observe by STEM and other methods, we based this conclusion on the experimental value of the center-to-center distance between the Ti_3C_2 sheets

[1]Department of Chemistry and James Franck Institute, University of Chicago, Chicago, IL 60637, USA. [2]Department of Physics, University of Illinois at Chicago, Chicago, IL 60607, USA. [3]Center for Nanoscale Materials, Argonne National Laboratory, Argonne, IL 60439, USA.
*Corresponding author. Email: dvtalapin@uchicago.edu

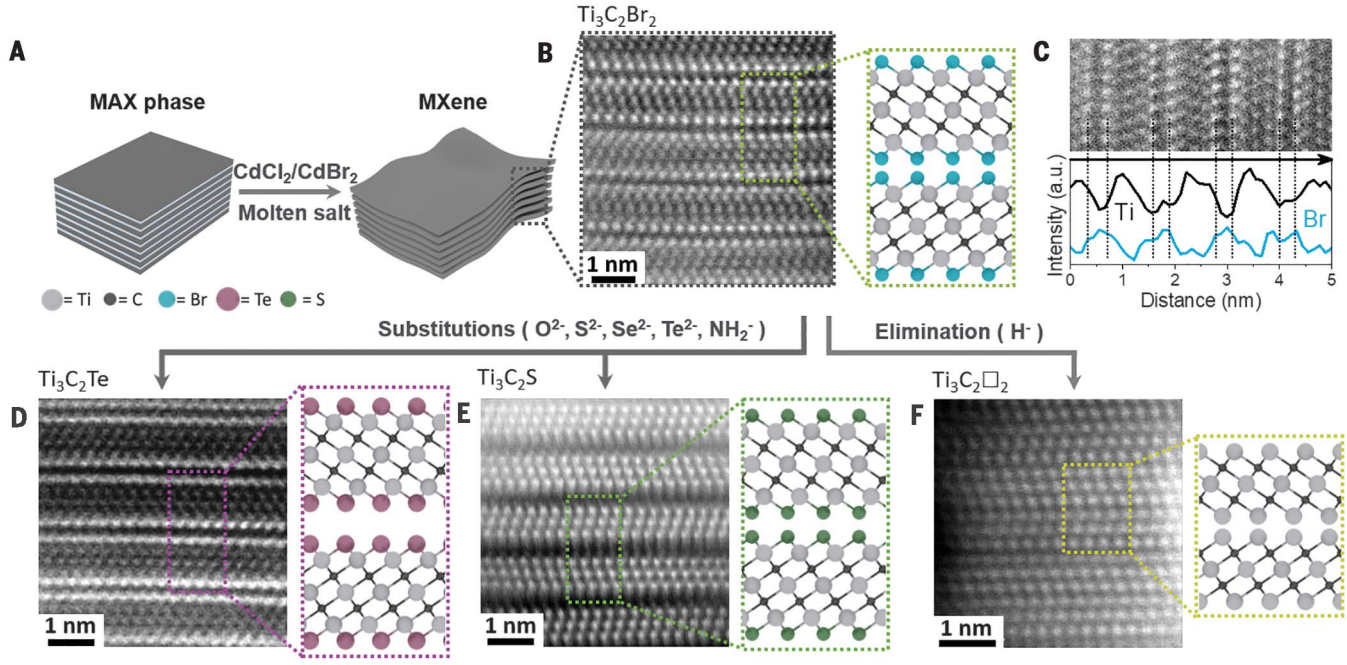

Fig. 1. Surface reactions of MXenes in molten inorganic salts. (**A**) Schematics for etching of MAX phases in Lewis acidic molten salts. (**B**) Atomic-resolution high-angle annular dark-field (HAADF) image of $Ti_3C_2Br_2$ MXene sheets synthesized by etching Ti_3AlC_2 MAX phase in $CdBr_2$ molten salt. The electron beam is parallel to the [$2\bar{1}\bar{1}0$] zone axis. (**C**) Energy-dispersive x-ray elemental analysis (line scan) of $Ti_3C_2Br_2$ MXene sheets. a.u., arbitrary units. HAADF images of (**D**) Ti_3C_2Te and (**E**) Ti_3C_2S MXenes obtained by substituting Br for Te and S surface groups, respectively. (**F**) HAADF image of $Ti_3C_2\square_2$ MXene ($\square$ stands for the vacancy) obtained by reductive elimination of Br surface groups.

(7.59 Å), which was substantially smaller than the theoretical prediction for $Ti_3C_2H_2$ MXene (8.26 Å) and near the smallest theoretically possible spacing of 7.23 Å (*21*). Because XPS showed reduction of Ti (fig. S16), this process could be formally described as a reductive elimination of the hydride groups after the exchange reaction.

The chemical transformations of solids are generally impeded by slow diffusion, which severely limits the scope of synthesizable solid-state compounds (*22*). The complete exchange of surface groups in stacked MXenes is also expected to be kinetically cumbersome, especially if the entering ions are bulkier than the leaving ones, as in the case of Cl^- (the ionic radius R_i = 1.81 Å) exchanged for Te^{2-} (R_i = 2.21 Å). Counterintuitively, the reactions of $Ti_3C_2Cl_2$ and Ti_2CCl_2 MXenes with O^{2-}, S^{2-}, Se^{2-}, and Te^{2-} occurred at similar temperatures and with comparable reaction rates.

To understand this reactivity, we followed the evolution of the (0002) diffraction peak during surface exchange reactions. In the initial state, $Ti_3C_2Cl_2$ sheets formed stacks (fig. S1) with d = 11.25 Å, and the van der Waals (vdW) gap between MXenes was ~2.8 Å (table S3), which is smaller than the dimensions of entering or leaving ions. No measurable changes of the d-spacing were detected upon heating $Ti_3C_2Cl_2$ in KCl-LiCl molten salt to 500°C (fig. S35). However, heating MXene in the same molten salt but in the presence of Li_2O resulted in d = 13.2 Å (fig. S36), which corresponds to a 4.7-to-6.3-Å vdW gap between the surface atoms on adjacent MXene sheets, depending on the local surface terminations (see supplementary materials). A similar d of 13.5 Å was observed during reaction of $Ti_3C_2Cl_2$ MXene with Li_2Se, although with a larger disorder (fig. S37).

The unstacking of MXene sheets in molten salts greatly facilitated diffusion of ions

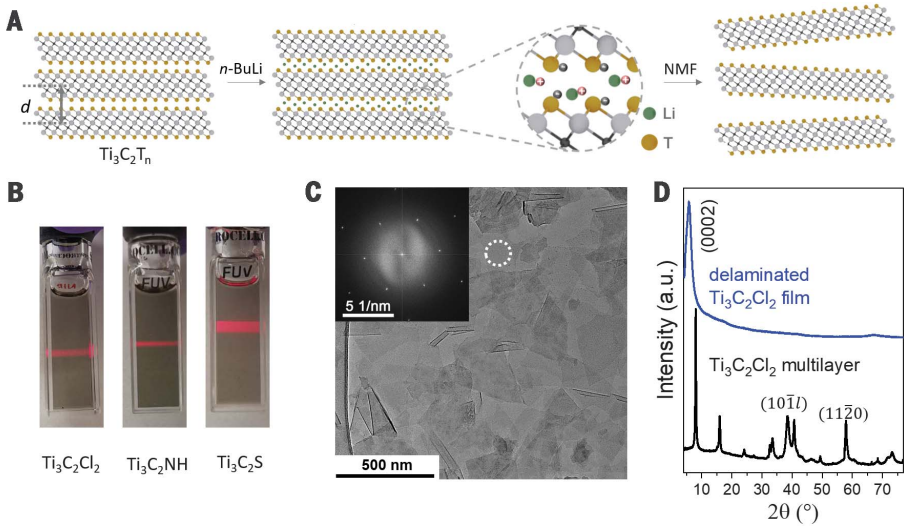

Fig. 2. Delamination of multilayer $Ti_3C_2T_n$ MXenes. (**A**) Schematic of delamination process. (**B**) Photographs of stable colloidal solutions of $Ti_3C_2T_n$ MXenes (T = Cl, S, NH) in NMF exhibiting Tyndall effect. (**C**) TEM image of $Ti_3C_2Cl_2$ MXene flakes deposited from a colloidal solution. (Inset) Fast Fourier transform of the circled region, showing crystallinity and hexagonal symmetry of the individual flake. (**D**) XRD patterns of multilayer MXene and delaminated flakes in a film spin coated on a glass substrate.

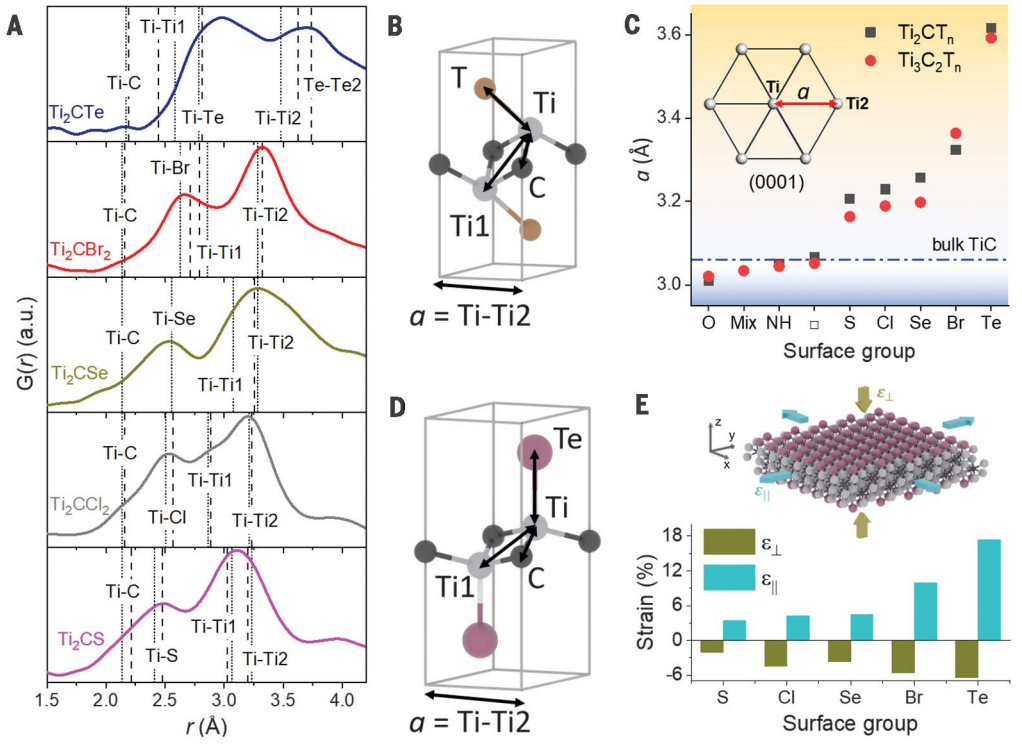

Fig. 3. Surface groups can induce giant strain in the MXene lattice. (**A**) Local interatomic distances in Ti_2CT_n MXenes (T = S, Cl, Se, Br, Te) probed by small *r* region of the atomic pair distribution functions, *G*(*r*). The vertical lines show the Ti-C and Ti-T bond lengths and Ti-Ti1 and Ti-Ti2 interatomic distances obtained from the Rietveld refinement of powder XRD patterns (dashed lines) and EXAFS analysis (dotted lines). (**B**) The unit cells of Ti_2CT_n MXenes (T = S, Cl, Se, Br) obtained from the Rietveld refinement. (**C**) Dependence of the in-plane lattice constant *a* [equivalent to the Ti-Ti2 distance in (A)] for Ti_2CT_n and $Ti_3C_2T_n$ MXenes on the chemical nature of the surface group (T_n). (**D**) Proposed unit cell of Ti_2CTe MXene (see fig. S39). (**E**) Biaxial straining of $Ti_3C_2T_n$ MXene lattice induced by the surface groups. The in-plane ($\varepsilon_{||}$) and out-of-plane ($\varepsilon_{\perp}$) strain components are evaluated with respect to the bulk cubic TiC lattice with a_{TiC} = 4.32 Å.

and made MXene surfaces sterically accessible. The interaction potential of MXenes in a molten salt was likely defined by surface-templated ion layering, which created an exponentially decaying oscillatory interaction energy (*23*). We speculate that the free energy released in the surface exchange reaction caused MXene sheets to "swell" into one of the energy minima and stay in this state during chemical transformation.

Moreover, the nature of the surface groups had an unusually strong impact on the MXene structure. The XRD patterns of $Ti_3C_2T_n$ and most of the Ti_2CT_n MXenes were modeled using the space group of the parent Ti_3AlC_2 and Ti_2AlC MAX phases ($P6_3/mmc$) (*24*). Because of the simpler structure of thinner Ti_2CT_n MXenes, their representative XRD patterns were further modeled using the Rietveld refinement. The fitting of the experimental Fourier-transformed EXAFS functions of Ti_2CT_n MXenes (fig. S26) demonstrated that the local structure around Ti atoms was consistent with the respective crystallographic models. The real-space interatomic PDFs, *G*(*r*), showed systematic shifts of Ti-T and Ti-Ti2 distances to larger values in S to Te series of Ti_2CT_n MXenes (Fig. 3, A and B, and fig. S27). In MXenes, the Ti-Ti2 distance is equal to the nearest-neighbor distance between Ti atoms in the basal (0001) plane, and hence it represents the in-plane *a* lattice constant (Fig. 3, B and C). For example, for Ti_2CBr_2, the Rietveld, EXAFS, and PDF methods converged on *a* = 3.32 Å. After exchanging Br^- for O^{2-}, the resultant MXene showed *a* = 3.01 Å, and the reaction with Te^{2-} produced MXene with *a* = 3.62 Å (Fig. 3C). The simulated XRD patterns of Ti_2CT_n MXenes (figs. S38 and S39) suggest that large Te^{2-} groups are likely positioned on top of the neighboring Ti atoms (Fig. 3D). This arrangement is distinctively different from the MXenes with smaller surface groups, which are positioned between hexagonally packed Ti surface atoms, on top of the opposite Ti atoms of the same Ti_2CT_n sheet (Fig. 3B), in accordance with recent theoretical studies (*25*).

The vdW radii and packing density of surface atoms had a huge effect on *a* (Fig. 3C), and fig. S40 compares these values with available computational predictions. For comparable ion radii, e.g., S versus Cl and Se versus Br, halido-terminated MXenes showed larger *a*, likely because of the smaller number of chalcogenide ions required for charge compensation of the MXene surface. To estimate the in-plane strain ($\varepsilon_{||}$) imposed on the titanium carbide lattice by surface groups in the newly synthesized MXene species, we compared *a* to the nearest-neighbor distance between Ti atoms in the (111) plane of bulk cubic TiC that is structurally equivalent to the basal (0001) MXene plane. For $Ti_3C_2T_n$ and Ti_2CT_n MXene families, the mixed (T_x = F, O, OH) and pure O^{2-} terminations resulted in a compressive $\varepsilon_{||}$. Bare (□) and NH-terminated MXenes were nearly strain-free, whereas Cl-, S-, Se-, and Br-terminated MXenes all had tensile $\varepsilon_{||}$. The thinner Ti_2CT_n MXenes had, on average, a slightly larger in-plane expansion or contraction with respect to the bulk TiC lattice than did the thicker $Ti_3C_2T_n$ MXenes. The Ti_2CTe MXene (Fig. 3, A and C, and fig. S24) had the largest magnitude of tensile $\varepsilon_{||}$ (18.2%), in accordance with Te^{2-} having the largest vdW radius among all groups used in this study. This degree of lattice expansion in a crystalline solid is very unusual. For comparison, the lattice of bulk TiC expands by only 2.5% when heated from room temperature to 2700°C (*26*).

Because the out-of-plane *c* lattice constant is strongly affected by the intercalation of ions and solvent molecules between MXene sheets (*27*), we used high-resolution STEM images to assess the distances between the Ti planes along the *c* axis of the unit cell (table S3). The magnitude of the out-of-plane strain in the MXene core ($\varepsilon_{\perp}$) was calculated by referencing experimental distances between Ti planes inside the MXene sheets ($M_{\perp}$) to the distance between the (111) planes of bulk TiC (table S3). Figure 3E shows that the expansion of the *a*-lattice parameter in $Ti_3C_2T_n$ MXenes functionalized with S, Cl, Se, Br, and Te atoms was accompanied by the corresponding contraction of the Ti_3C_2 layers along the *c* axis.

This observation is consistent with the behavior of the Ti_3C_2 layers as an elastic 2D sheet under tensile stress imposed by the surface atoms (Fig. 3E). The Poisson effect can account for the relations between the stress and the strain components reflected by

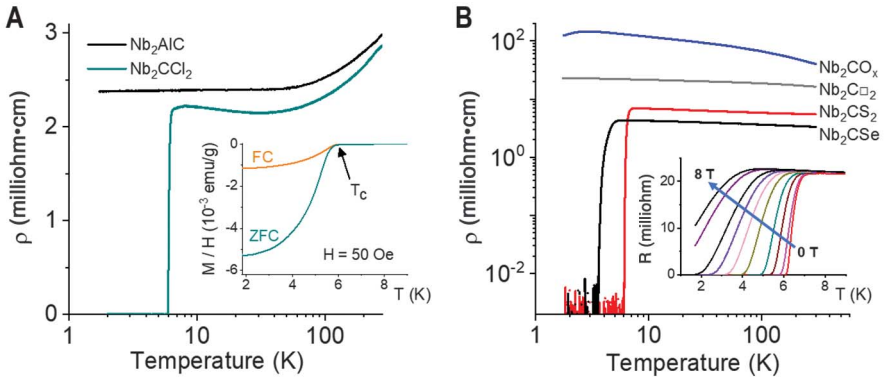

Fig. 4. Electronic transport and superconductivity in Nb_2CT_n MXenes. (**A**) Temperature-dependent resistivity for the cold-pressed pellets of Nb_2AlC MAX phase and Nb_2CCl_2 MXene. (Inset) Magnetic susceptibility (i.e., ratio of magnetization to magnetizing field strength) of Nb_2CCl_2 MXene as a function of temperature. FC and ZFC correspond to the field cooled and zero-field cooled measurements, respectively. emu, electromagnetic unit. (**B**) Temperature-dependent resistivity for the cold-pressed pellets of Nb_2CT_n MXenes. (Inset) Resistance as a function of temperature at different applied magnetic fields (0 to 8 T) for the cold-pressed pellets of Nb_2CS_2 MXene.

observed changes of a and $M_\perp$ distances. Unfortunately, our atomic-resolution STEM images of MXenes measured $M_\perp$ values with relatively large error bars (caused by projection effects and bending of the MXene sheets), which interfered with accurate estimation of the Poisson's ratio (ν) for newly synthesized MXenes. A simple elastic model (see supplementary materials) applied to $Ti_3C_2T_n$ yields ν ~ 0.22 for T = S and Br, which is comparable to the recently predicted ν value for $Ti_3C_2T_x$ (*21*). However, Ti_3C_2Te showed ν = 0.16 ± 0.06, likely caused by the additional stiffening of the Ti_3C_2 layers under very large in-plane stress.

The above examples show that the composition and structure of MXenes can be engineered with previously unattainable versatility. Chemical functionalization of MXene surfaces is expected to affect nearly every property of these materials, and we found that the surface groups defined the nature of electronic transport in Nb_2CT_n MXenes. Figure 4, A and B, shows temperature-dependent four-probe resistivity (ρ) measured on cold-pressed pellets of Nb_2CT_n (T = □, Cl, O, S, Se) MXenes (fig. S41), all synthesized by the procedures described above. Figure 4A also compares the conductivity of the parent Nb_2AlC MAX phase with that of Nb_2CCl_2 MXene. Above 30 K, both MAX phase and MXene samples showed similar specific resistivity, which decreased when the sample was cooled. This temperature dependence is often associated with metallic conductivity. The ultraviolet photoelectron spectroscopy (UPS) confirmed nonzero density of electronic states at the Fermi energy E_F (fig. S42), which is also consistent with a metallic state.

However, when the Nb_2CCl_2 MXene was cooled below 30 K, the resistivity started increasing, possibly indicating the onset of localization. A sharp drop of resistivity by several orders of magnitude occurred at a critical temperature T_c ~ 6.0 K (Fig. 4A), which is reminiscent of a superconductive transition. The magnetic susceptibility measurements showed the development of a strong diamagnetism below 6.3 K that we interpreted as the Meissner effect (Fig. 4A). From the magnitude of zero-field cooled data at 1.8 K, we estimated the lower bound for the superconducting volume fraction of Nb_2CCl_2 MXene as ~35%. Consistent with superconductivity, the transition broadened, and T_c shifted to lower temperatures with the application of an external magnetic field (Fig. 4B and fig. S43). In contrast, the parent Nb_2AlC MAX phase exhibited normal metal behavior down to the lowest measured temperature (1.8 K), which is consistent with a previously reported T_c ~ 0.44 K for Nb_2AlC (*28*). For reference, Nb_2CT_x MXene with mixed O, OH, and F termination prepared by the traditional aqueous HF etching route shows two orders of magnitude higher resistivity and no superconductivity (fig. S44) (*29*).

In contrast to the Nb_2CCl_2 MXene, the resistivity of MXenes terminated with chalcogenide ions (O, S, Se) gradually increased when the sample was cooled (Fig. 4B), which is consistent with the activated transport regime. Given that UPS showed the finite density of states at E_F in Nb_2CS_2 (fig. S42), we hypothesized that the localization was controlled by the tunneling rates for charge carriers between metallic MXene sheets. The oxo-terminated Nb_2CT_n MXene showed the highest resistivity, and the seleno-terminated MXene showed the lowest resistivity, consistent with the reduction of the tunneling barrier heights between the MXene sheets.

In the low-temperature region, we observed superconducting transitions in Nb_2CS_2 (T_c ~ 6.4 K), Nb_2CSe (T_c ~ 4.5 K), and $Nb_2C(NH)$ (T_c ~ 7.1 K) (fig. S34), whereas Nb_2CO_x did not enter the superconducting state (fig. S45). In granular metals, the development of macroscopic superconductivity can be suppressed by weak coupling of individual superconducting domains, which is also reflected by the high resistivity in the normal state (*30*). The upper critical field (μ_0H_{c2}) showed a strong dependence on the surface functional group. For example, Nb_2CS_2 MXene exhibited higher μ_0H_{c2} compared with Nb_2CCl_2 (Fig. 4B, inset, and fig. S46). Bare $Nb_2C□_2$ MXenes, on the other hand, showed no transition to the superconducting state down to 1.8 K (Fig. 4B). Thus, surface groups were not spectators but active contributors to the MXene superconductivity, which is consistent with surface groups affecting biaxial lattice strain, phonon frequencies, and the strength of electron-phonon coupling.

The MXene exchange reactions represent an exciting counterexample to the traditional perception of solids as entities that are difficult to postsynthetically modify. We showed that chemical bonds inside an extended MXene stack can be rationally designed in a way that is more typical for molecular compounds. Other MXene structures could be enabled by the combinations of etching and substitution reactions using Lewis acidic and Lewis basic molten salts, respectively.

REFERENCES AND NOTES

1. B. Anasori, M. R. Lukatskaya, Y. Gogotsi, *Nat. Rev. Mater.* **2**, 16098 (2017).
2. Y. Xia *et al.*, *Nature* **557**, 409–412 (2018).
3. C. J. Zhang *et al.*, *Nat. Commun.* **10**, 849 (2019).
4. F. Shahzad *et al.*, *Science* **353**, 1137–1140 (2016).
5. V. Kamysbayev *et al.*, *ACS Nano* **13**, 12415–12424 (2019).
6. J. Guo *et al.*, *Adv. Mater.* **30**, e1801846 (2018).
7. J. Zhang *et al.*, *Nat. Catal.* **1**, 985–992 (2018).
8. M. Khazaei *et al.*, *Adv. Funct. Mater.* **23**, 2185–2192 (2013).
9. L. Zhou, Y. Zhang, Z. Zhuo, A. J. Neukirch, S. Tretiak, *J. Phys. Chem. Lett.* **9**, 6915–6920 (2018).
10. Y. Liu, H. Xiao, W. A. Goddard 3rd, *J. Am. Chem. Soc.* **138**, 15853–15856 (2016).
11. C. Si, J. Zhou, Z. Sun, *ACS Appl. Mater. Interfaces* **7**, 17510–17515 (2015).
12. S.-Y. Pang *et al.*, *J. Am. Chem. Soc.* **141**, 9610–9616 (2019).
13. T. Li *et al.*, *Angew. Chem. Int. Ed.* **57**, 6115–6119 (2018).
14. M. Li *et al.*, *J. Am. Chem. Soc.* **141**, 4730–4737 (2019).
15. Y. Li *et al.*, *Nat. Mater.* **19**, 894–899 (2020).
16. D. Kim *et al.*, *ACS Nano* **13**, 13818–13828 (2019).
17. V. Srivastava *et al.*, *J. Am. Chem. Soc.* **140**, 12144–12151 (2018).
18. A. Dash, R. Vaßen, O. Guillon, J. Gonzalez-Julian, *Nat. Mater.* **18**, 465–470 (2019).
19. X. Liu, N. Fechler, M. Antonietti, *Chem. Soc. Rev.* **42**, 8237–8265 (2013).

20. M. Ghidiu, M. W. Barsoum, *J. Am. Ceram. Soc.* **100**, 5395–5399 (2017).
21. Z. H. Fu *et al.*, *Phys. Rev. B* **94**, 104103 (2016).
22. M. Jansen, *Angew. Chem. Int. Ed.* **41**, 3746–3766 (2002).
23. H. Zhang *et al.*, *Nature* **542**, 328–331 (2017).
24. M. Sokol, V. Natu, S. Kota, M. W. Barsoum, *Trends Chem.* **1**, 210–223 (2019).
25. Y. Qin *et al.*, *J. Phys. Condens. Matter* **32**, 135302 (2019).
26. J. H. Richardson, *J. Am. Ceram. Soc.* **48**, 497–499 (1965).
27. O. Mashtalir *et al.*, *Nat. Commun.* **4**, 1716 (2013).
28. T. H. Scabarozi *et al.*, *Thin Solid Films* **517**, 2920–2923 (2009).
29. J. Halim *et al.*, *J. Phys. Condens. Matter* **31**, 165301 (2019).
30. I. S. Beloborodov, A. V. Lopatin, V. M. Vinokur, K. B. Efetov, *Rev. Mod. Phys.* **79**, 469–518 (2007).

ACKNOWLEDGMENTS

We thank Y. Gogotsi and B. Anasori (Drexel University) for sharing the early samples of Ti_3AlC_2 MAX phase and introducing us to the exciting field of MXenes. T. Witten, J. Anderson, J. Park, and B. Tian (University of Chicago) are acknowledged for many stimulating discussions. We also thank C. Malliakas (Northwestern University) and A. Yakovenko [17-BM-B, Advanced Photon Source (APS)] for transmission powder XRD, O. Borkiewicz (11-ID-B, APS) for x-ray total scattering, C.-J. Sun (20-BM-B, APS) for XAS, and J. Xie (University of Chicago) for magnetization measurements. **Funding:** V.K., H.H., D.W., and D.V.T. were supported by the Department of Defense (DOD) Air Force Office of Scientific Research grant FA9550-18-1-0099; by the Office of Basic Energy Sciences, U.S. Department of Energy, award no. DE-SC0019375; and by the National Science Foundation awards nos. DMR-1611371 and DMR-2004880. X.R., F.L., and R.F.K. were supported by the National Science Foundation (DMREF CBET-1729420). The JEOL JEM ARM200CF in the UIC Research Resources Center was acquired and upgraded using grants from the National Science Foundation (DMR-0959470 and DMR-1626065). This research used resources of the Center for Nanoscale Materials and the Advanced Photon Source, an Office of Science User Facilities operated for the U.S. Department of Energy (DOE) Office of Science by Argonne National Laboratory, supported by the U.S. DOE under contract no. DE-AC02-06CH11357, and the Canadian Light Source and its funding partners. **Author contributions:** V.K. designed and performed the experiments, analyzed data, and cowrote the paper. A.S.F. contributed to the x-ray data analysis. X.R., F.L., and R.F.K. performed high-resolution STEM studies and image analysis. H.H. and D.W. carried out MAX phase synthesis and delamination of MXenes. D.V.T. conceived of and designed experiments, analyzed data, cowrote the paper, and supervised the project. All authors discussed the results and commented on the manuscript. **Competing interests:** V.K. and D.V.T. are inventors on patent application U.S. 63/020,885 submitted by the University of Chicago, which covers surface modifications of MXenes and methods. **Data and materials availability:** All data needed to evaluate the conclusions in the paper are present in the paper or the supplementary materials.

SUPPLEMENTARY MATERIALS

science.sciencemag.org/content/369/6506/979/suppl/DC1
Materials and Methods
Supplementary Text
Figs. S1 to S46
Tables S1 to S15
References (*31*–*59*)

9 January 2020; accepted 2 June 2020
Published online 2 July 2020
10.1126/science.aba8311

Science

Covalent surface modifications and superconductivity of two-dimensional metal carbide MXenes

Vladislav Kamysbayev, Alexander S. Filatov, Huicheng Hu, Xue Rui, Francisco Lagunas, Di Wang, Robert F. Klie and Dmitri V. Talapin

Science **369** (6506), 979-983.
DOI: 10.1126/science.aba8311originally published online July 2, 2020

Modifying MXene surfaces

Unlike graphene and transition-metal dichalcogenides, two-dimensional transition-metal carbides (MXenes) have many surface sites that can be chemically modified. Etching of the aluminum layer of a parent MAX phase Ti_3AlC_2 layered material with hydrofluoric acid leads to the MXene Ti_3C_2 with various surface terminations. Molten salts can achieve uniform chloride terminations, but these are difficult to further modify. Kamysbayev *et al.* show that etching of MAX phases in molten cadmium bromide leads to bromide-terminated MXenes that can then be substituted with oxygen, sulfur, selenium, tellurium, and NH groups as well as with vacancy sites. The surface groups can alter electronic transport. For example, the Nb_2C MXenes exhibit surface group–dependent superconductivity.

Science, this issue p. 979

Science (print ISSN 0036-8075; online ISSN 1095-9203) is published by the American Association for the Advancement of Science, 1200 New York Avenue NW, Washington, DC 20005. The title *Science* is a registered trademark of AAAS.